Journal of Alloys and Compounds 747 (2018) 1078–1087

Contents lists available at ScienceDirect

Journal of Alloys and Compounds

journal homepage: http://www.elsevier.com/locate/jalcom

Influence Ca-doped $SrIn_2O_4$ powders on photoluminescence property prepared one step by ultrasonic spray pyrolysis

P.N. Medeiros [a], A.A.G. Santiago [b], E.A.C. Ferreira [b], M.S. Li [c], E. Longo [d], M.R.D. Bomio [b], F.V. Motta [b, *]

[a] IFBA, Instituto Federal da Bahia - Campus Jacobina, 44700-000 Jacobina, BA, Brazil
[b] LSQM, Laboratório de Síntese Química de Materiais - DEMat, Universidade Federal do Rio Grande do Norte - UFRN, P.O. Box 1524, 59078-970 Natal, RN, Brazil
[c] IFSC, USP, Av. Trabalhador São Carlense, 400, CEP 13566-590 São Carlos, SP, Brazil
[d] CDMF-UFSCar, Universidade Federal de São Carlos, P.O. Box 676, 13565-905 São Carlos, SP, Brazil

ARTICLE INFO

Article history:
Received 30 January 2018
Accepted 8 March 2018
Available online 9 March 2018

Keywords:
Ultrasonic spray pyrolysis
Indate
Strontium
Optical properties
Photoluminescence

ABSTRACT

Crystalline Ca-doped $SrIn_2O_4$ structures were prepared by a rapid and efficient Ultrasonic Pyrolysis Spray (USP) method. The $Sr_{1-x}Ca_xIn_2O_4$ (x = 0, 0.1, 0.2, 0.3, 0.4 and 1 mol %) samples were obtained by in a single step at a temperature of 1050 °C for 1 min for the formation of particles. The powders were characterized by X-ray diffraction (XRD), field emission electron microscopy (SEM-FEG), optical diffuse reflectance and photoluminescence (PL) measurements. All diffraction peaks present in XRD patterns could be indexed to the orthorhombic structure and that with calcium percentage increments indicates the substitution of Ca^{2+} in the Sr^{2+} sites promotes a decrease in its lattice parameters of the structure. MEV-FEG images show that the $Sr_{1-x}Ca_xIn_2O_4$ particles have a spherical predominance, with a porous surface in the form of foam for x = 0 and a surface with low roughness and low porosity with an increase in the percentage of Ca^{2+} ion, especially for the 1 mol % of Ca^{2+}. The gap energy varied between 4.56 eV and 4.86 eV, being influenced by the structural modifications motivated by increase of Ca^{2+} ion contained in the $SrIn_2O_4$ matrix. The PL emission spectrum of the samples presents a broad band behavior with emission intensity predominant in the blue-green region, having the sample with x = 0.1 the highest PL intensity. The chromaticity coordinates were calculated for the sample based on the PL spectrum and coordinates x and y show that the samples have blue emission. Ultrasonic spray pyrolysis was an effective technique for Ca-doped SrInO4 powder production using short production times with hold great potential for photoluminescent emitters.

1. Introduction

Indium-based oxides have been constantly investigated, due to their probable applications in photocatalysis [1–5], solar cells [6], gas sensors [7,8], anode lithium ion batteries [9] and phosphors [10,11].

$SrIn_2O_4$ is a semiconductor that has an orthorhombic structure of the $CaFe_2O_4$ type with Pnam (D_{2h}^{16}) space group [12]. In the $SrIn_2O_4$ structure, there are octahedral chains of InO_6, which give this material good photocatalytic and luminescent properties due to a possible mobility of charge carriers [13]. Kang et al. [14] obtained $SrIn_2O_4$ doped with $Eu^{3+}$and studied the photoluminescent properties in the application of red phosphors to white LED's. Wang and Tian [15] investigated the photoluminescent properties of $SrIn_2O_4$:Eu^{3+},Gd^{3+}e $SrIn_2O_4$:Eu^{3+},Sm^{3+}. Li et al. [16] synthesized $SrIn_2O_4$ 4: Eu^{3+}, Sm^{3+} and observed some red emission in the photoluminescent spectrum. Kao [17] obtained yellow-green phosphors from $SrIn_2O_4$ powders:xTb. Photocatalytic properties and luminescent upconversion of $SrIn_2O_4$ are also reported in the literature [18–20].

$CaIn_2O_4$ is a semiconductor that presents an orthorhombic crystal structure also of the $CaFe_2O_4$ type but with space group *Pca*2_1 or *Pbcm* [21]. Studies on the photoluminescent properties of $CaIn_2O_4$ have been reported in the literature, such as obtaining orange-red [21] and white-hot [22] and effective upconversion

* Corresponding author. LSQM, Laboratório de Síntese Química de Materiais - DEMat, Universidade Federal do Rio Grande do Norte - UFRN, P.O. Box 1524, 59078-970 Natal, RN, Brazil.
E-mail address: fabiana@ct.ufrn.br (F.V. Motta).

https://doi.org/10.1016/j.jallcom.2018.03.090
0925-8388/

[23–25].

The solid-state reaction method is commonly used to obtain the indates (MIn_2O_4, M = Ca, Sr, Ba), but it is a method that uses very high temperatures and long furnace periods [13–15,26,27]. Other more energy-efficient methods of obtaining indates are reported in the literature, such as combustion method [16,28], coprecipitation [29], electrospinning [30], pechini sol-gel [31] and spray pyrolysis [32,33].

The ultrasonic pyrolysis spray (USP) method consists of atomising or nebulizing a precursor solution by ultrasound, then the droplets undergo thermal treatment, suffering physicochemical phenomena such as solvent evaporation, precipitation and drying of the solutes for the formation of fine powders, occurring the need for decomposition or chemical alteration by reduction or oxidation of these fine powders with morphology of non-agglomerated microspheres [34,35].

In this work, $Sr_{1-x}Ca_xIn_2O_4$ powders (x = 0, 0.1, 0.2, 0.3, 0.4 and 1 mol %) were obtained in a single step by ultrasonic pyrolysis spray method (USP). The time for particle formation inside the reactor was approximately 1 min. The correlation of the photoluminescent properties with doped Ca ions are substituted for the Sr ions in the $SrIn_2O_4$ crystal structure was investigated.

2. Experimental

2.1. Materials

$Sr_{1-x}Ca_xIn_2O_4$ (x = 0, 0.1, 0.2, 0.3, 0.4 and 1 mol %) powders were prepared by the ultrasonic spray pyrolysis method (USP) [36,37]. Indium nitrate [In $(NO_3)_2$. (Alfa Aesar, 99% purity), and calcium nitrate tetrahydrate [$Ca(NO_3)_2$] (Alfa Aesar, 99% purity). $4H_2O$] (Synth, 99% purity) were used as precursors.

2.2. Preparation of $Sr_{1-x}Ca_xIn_2O_4$ particles

The precursor solution was prepared by dissolving 9 mmol of strontium nitrate and 18 mmol of indium nitrate in 190 ml of distilled water. The precursor solution was atomized using an ultrasonic nebulizer with a frequency of 2.4 MHz. The nebulizer was coupled in a quartz aerosol reactor of laminar flow (50 mm in diameter and 1.2 m in length). The reactor was inserted into a horizontal electric double tubular heating furnace. The atomized droplets were transported inside the reactor by an air flow, at an air flow rate of 3 L min-1. The heating temperatures were 700 °C for zone 1 and 1050 °C for zone 2. The resulting particles were collected by means of electrostatic precipitation at the end of the reactor by a copper tube. The other precursor solutions (x = 0.1, 0.2, 0.3, 0.4 and 1 mol %) were performed according to stoichiometry.

2.3. Characterization of $Sr_{1-x}Ca_xIn_2O_4$ particles

The $Sr_{1-x}Ca_xIn_2O_4$ powders (x = 0, 0.1, 0.2, 0.3, 0.4 and 1 mol %) were characterized by XRD 7000, 30 kV and 30 mAh XRD (Shimadzu, model XRD 7000) with CuKα radiation (λ = 1.5406 Å), 2θ 10° to 80° and step speed of 1° min^{-1}. The morphology was analyzed using field emission scanning electron microscopy (SEM-FEG) (Carl Zeiss, model Supra 35-VP) operating at 6 kV. The Uv–vis reflectance spectrum was obtained using Uv–Vis spectrometer (Shimadzu, model UV-2600). Photoluminescence (PL) spectra were obtained using a 27 Thermal Jarrell-Ash Monospec monochromator and an R446 Hamamatsu photomultiplier. The excitation source used in the samples was a laser with a wavelength of 350.7 nm with krypton ions (Coherent Innova) with an output of approximately 13.3 mW.

3. Results and discussion

Fig. 1 shows the XRD patterns of the $Sr_{1-x}Ca_xIn_2O_4$ (x = 0, 0.1, 0.2, 0.3, 0.4 and 1 mol %) powders obtained by the ultrasonic pyrolysis spray method. The samples were indexed in a unit cell with orthorhombic structure with the space group P*nam* (66) according to JCPDS 33–1336. While the samples with x = 1 were indexed in a unit cell with orthorhombic structure with the space group P*ca* (57) according to JCPDS 17–0643. The presence of $SrCO_3$ peaks was observed. The formation of $SrCO_3$ is attributed by the reaction between SrO and carbon dioxide under a low oxygen partial pressure and at high temperatures [31]. No other peaks were observed regarding possible secondary phases of calcium, thus indicating that the indates were well crystallized by the Ultrasonic Pyrolysis Spray (USP) method and that the Ca^{2+} were well incorporated in the $SrIn_2O_4$ structure, forming a solid solution. With the increase of the calcium percentage in the orthorhombic phase of $SrIn_2O_4$obtained by UPS (Fig. 1II), it was verified that a small displacement of the diffraction peaks occurs to larger angles (2θ), indicating a decrease in the network parameters of the material, which is attributed to the substitution of Ca^{2+} ions at the Sr^{2+} sites.

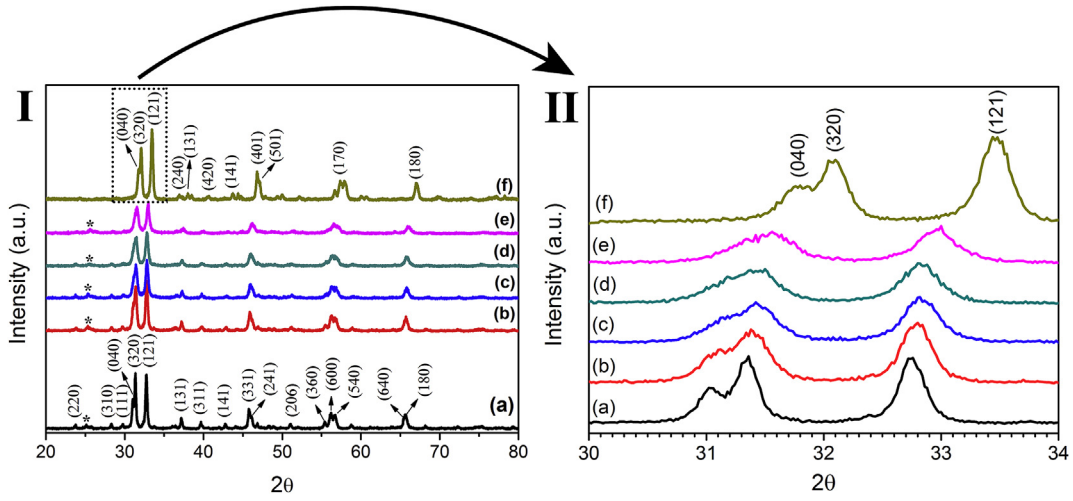

Fig. 1. XRD patterns of $Sr_{1-x}Ca_xIn_2O_4$ obtained by USP with (a) x = 0, (b) x = 0.1, (c) x = 0.2, (d) x = 0.3, (e) x = 0.4 and (f) x = 1. [*: $SrCO_3$ (JCPDS 84–1778)].

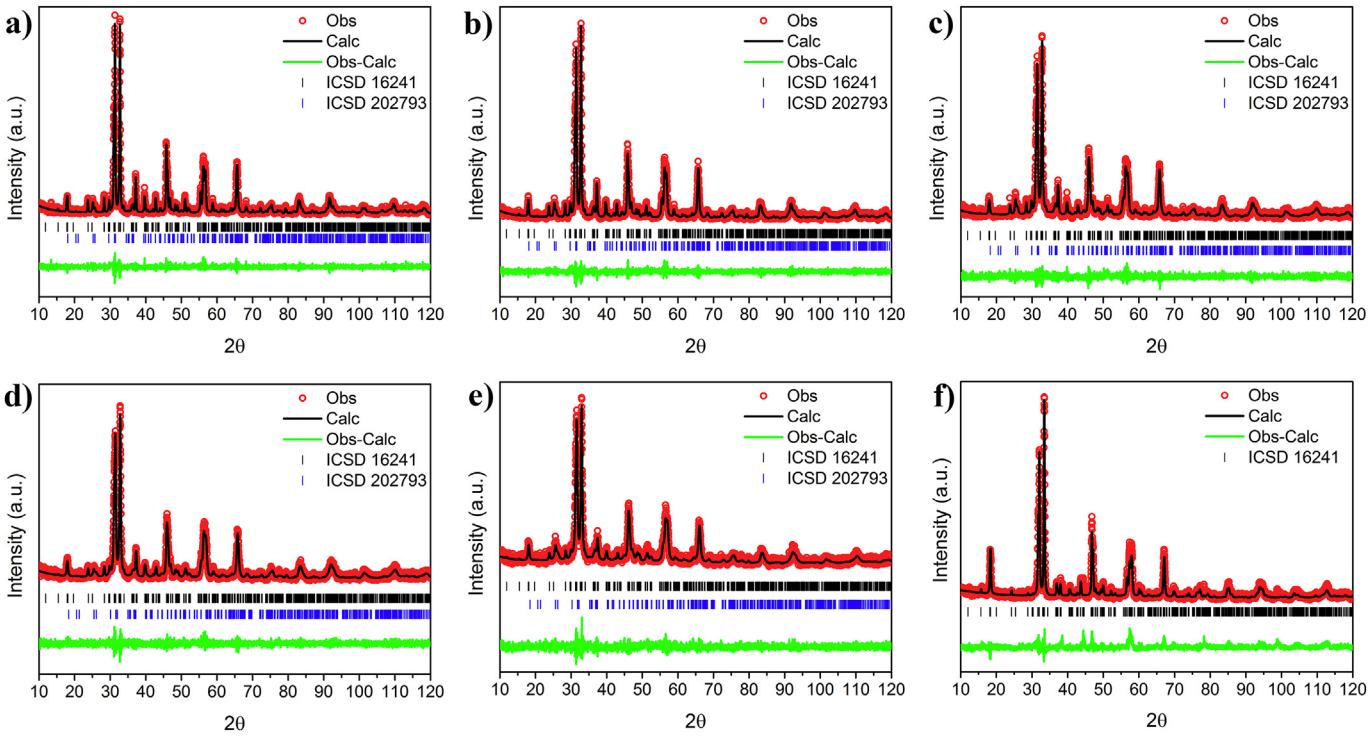

Fig. 2. Rietveld refinement of $Sr_{1-x}Ca_xIn_2O_4$ with (a) x = 0, (b) x = 0.1, (c) x = 0.2, (d) x = 0.3, (e) x = 0.4 and (f) x = 1.

Ramarao et al. [38] replaced $Ca^{2+}$for Sr^{2+}ions in a Mo matrix and observed similar behavior, with shifting to smaller angles and increasing network parameters.

In order to explain possible modifications of the differences in the structural arrangements induced by the processing of $Sr_{1-x}Ca_xIn_2O_4$ particles the Rietveld refinement method [39] was performed using the General Structure Analysis System (GSAS) program with the EXPGUI graphical interface [40]. Since no correct ICSD or JCPDS file is available for $CaIn_2O_4$, all peaks $Sr_{1-x}Ca_xIn_2O_4$ were indexed by orthorhombic cells (*Pnma*) with parameters close to 16241 ICSD ($SrIn_2O_4$) [20]. The refined parameters were as follows: scale factor and phase fraction; background, which was modeled using a displaced Chebyshev polynomial function; peak shape, which was modeled using Thomson-Cox-Hasting pseudo-Voigt; change in network constants; fractional atomic coordinates; and isotropic thermal parameters. The results of the Rietveld refinement are shown in Fig. 2.

For the samples the diffraction patterns are well adapted to 16241 ICSD. As shown in the Obs-Calc line, the differences between the experimentally observed diffraction patterns and the theoretically calculated data are close to zero. Tables 1 and 2 present the results of the structural parameters and atomic positioning, crystallite size of $Sr_{1-x}Ca_xIn_2O_4$, obtained by refinement. For x = 0 and 1, the values found for the network parameters, *a*, *b* and *c*, are in agreement with the literature. Lakshminarasimhan and Varadaraju [41] synthesized $SrIn_2O_4$ by the solid state reaction method at 1200 °C for 24 h and obtained the values for the network parameters *a* = 9.8082 Å, *b* = 11.4578 Å and *c* = 3.2581 Å. Guan et al. [20] obtained $CaIn_2O_4$ via a solid state reaction at 1300 °C for 3 h, resulting in the values of *a* = 9.6485 Å, *b* = 11.2953 Å and *c* = 3.2144 Å. In this work, the Ca^{2+} ions that substitute the Sr^{2+} ions, show a decrease in the ionic radius in the following sequence: Sr^{2+}(0.126 nm) > Ca^{2+}(0.112 nm). Thus, the network parameters decrease with the increase of the Ca^{2+} ion contained in the $SrIn_2O_4$ matrix (Table 1), according to the literature [38].

The $Sr_{1-x}Ca_xIn_2O_4$ crystallite size decreased from 41 nm (x = 0)

Table 1
Rietveld refined structural parameters for the$Sr_{1-x}Ca_xIn_2O_4$ (with x = 0, 0.1, 0.2, 0.3, 0.4 and 1).

Compounds	$SrIn_2O_4$	$Sr_{0.9}Ca_{0.1}In_2O_4$	$Sr_{0.8}Ca_{0.2}In_2O_4$	$Sr_{0.7}Ca_{0.3}In_2O_4$	$Sr_{0.6}Ca_{0.4}In_2O_4$	$CaIn_2O_4$
Crystal system	Orthorhombic	Orthorhombic	Orthorhombic	Orthorhombic	Orthorhombic	Orthorhombic
Space Group	*Pnam*	*Pnam*	*Pnam*	*Pnam*	*Pnam*	*Pnam*
Lattice parameters (Å)						
a	9.8430	9.8312	9.8157	9.8051	9.7901	9.6538
b	11.5178	11.5089	11.4895	11.4819	11.4508	11.3005
c	3.2740	3.2728	3.2689	3.2675	3.2607	3.2197
α	90°	90°	90°	90°	90°	90°
V(Å³)	371.179	370.316	368.672	367.867	365.553	351.242
X^2	1.229	1.210	1.203	1.203	1.224	1.946
Rwp (%)	18.75	17.96	18.30	19.41	19.34	17.84
Rp (%)	13.77	13.06	13.39	14.38	14.43	13.91
D (nm)	41.4762	31.0655	24.8951	26.2382	22.8719	35.2113
ε (x10⁻³)	1.1083	1.5590	1.0904	2.6944	2.2348	1.5213

Table 2
Position of the atoms in the unit cell.

Sample	Atom	x	y	z	Occ
$SrIn_2O_4$	Sr1	0.7548	0.6523	0.2500	1.0000
	In1	0.4183	0.1070	0.2500	1.0000
	In2	0.4291	0.6113	0.2500	1.0000
	O1	0.2151	0.1651	0.2500	1.0000
	O2	0.1308	0.4769	0.2500	1.0000
	O3	0.5214	0.7800	0.2500	1.0000
	O4	0.4066	0.4188	0.2500	1.0000
$Sr_{0.9}Ca_{0.1}In_2O_4$	Sr1	0.7536	0.6533	0.2500	0.9288
	In1	0.4195	0.1075	0.2500	1.0000
	In2	0.4295	0.6119	0.2500	1.0000
	O1	0.1290	0.1675	0.2500	1.0000
	O2	0.1290	0.4655	0.2500	1.0000
	O3	0.5275	0.7761	0.2500	1.0000
	O4	0.4054	0.4256	0.2500	1.0000
	Ca1	0.7536	0.6533	0.2500	0.1032
$Sr_{0.8}Ca_{0.2}In_2O_4$	Sr1	0.7529	0.6535	0.2500	0.8457
	In1	0.4179	0.1086	0.2500	1.0000
	In2	0.4285	0.6123	0.2500	1.0000
	O1	0.2114	0.1684	0.2500	1.0000
	O2	0.1347	0.4623	0.2500	1.0000
	O3	0.5504	0.7634	0.2500	1.0000
	O4	0.4074	0.4274	0.2500	1.0000
	Ca1	0.7529	0.6535	0.2500	0.2112
$Sr_{0.7}Ca_{0.3}In_2O_4$	Sr1	0.7533	0.6541	0.2500	0.7798
	In1	0.4190	0.1082	0.2500	1.0000
	In2	0.4282	0.6122	0.2500	1.0000
	O1	0.2094	0.1674	0.2500	1.0000
	O2	0.1304	0.4704	0.2500	1.0000
	O3	0.5236	0.7824	0.2500	1.0000
	O4	0.3985	0.4247	0.2500	1.0000
	Ca1	0.7533	0.6541	0.2500	0.3344
$Sr_{0.6}Ca_{0.4}In_2O_4$	Sr1	0.7504	0.6509	0.2500	0.6589
	In1	0.4168	0.1087	0.2500	1.0000
	In2	0.4283	0.6129	0.2500	1.0000
	O1	0.2056	0.1685	0.2500	1.0000
	O2	0.1435	0.4415	0.2500	1.0000
	O3	0.5596	0.7605	0.2500	1.0000
	O4	0.4106	0.4354	0.2500	1.0000
	Ca1	0.7504	0.6509	0.2500	0.4396
$CaIn_2O_4$	Ca1	0.7540	0.6487	0.2500	1.0000
	In1	0.4182	0.1086	0.2500	1.0000
	In2	0.4269	0.6124	0.2500	1.0000
	O1	0.2080	0.1942	0.2500	1.0000
	O2	0.1450	0.4591	0.2500	1.0000
	O3	0.5090	0.7964	0.2500	1.0000
	O4	0.3890	0.4143	0.2500	1.0000

to 23 nm (x = 0.4) (Table 1). This behavior can be explained by the fact that the increase in the Ca percentage was accompanied by the increase in the number of defects of the crystalline strontium-induced lattice, which increased the network tension (Ca^{2+} and Sr^{2+} cations and O^{2-}interstitial anions, respectively). This behavior is a reminiscent of Vegard's law, which for two-component metal solid solutions, predicts that the unit cell dimensions of the solid solution vary linearly with the concentration of the solute component [42,43].

The reliability parameters X^2, R_{wp} and R_p, shown in Table 1, indicate a good quality of structural refinements and numerical results. These data confirm that the $Sr_{1-x}Ca_xIn_2O_4$ samples (with x = 0, 0.1, 0.2, 0.3, 0.4 and 1) show a crystalline structure which is suitably described by an orthorhombic structure, with symmetry described by the P*nam* space group. In addition, it was also observed the presence of $SrCO_3$ secondary phase for all compositions investigated. The percentages of each phase are shown in Table 3.

With the network parameter data and atomic coordinate data obtained in the Rietveld refinement (Tables 1 and 2), the VESTA program [44] was used to model the unit cells of each sample, as shown in Fig. 3.

Table 3
Percentage of each phase obtained by Rietveld refinement.

Sample	$SrIn_2O_4$ (ICSD 16241)	$SrCO_3$ (ICSD, 202793)
$SrIn_2O_4$	89.98%	10.02%
$Sr_{0.9}Ca_{0.1}In_2O_4$	87.15%	12.85%
$Sr_{0.8}Ca_{0.2}In_2O_4$	85.64%	14.36%
$Sr_{0.7}Ca_{0.3}In_2O_4$	88.11%	11.89%
$Sr_{0.6}Ca_{0.4}In_2O_4$	82.38%	17.62%

The $Sr_{1-x}Ca_xIn_2O_4$ orthorhombic structure (*Pnma*) is formed of two different octahedron clusters of [InO_6] and one octahedrode cluster [SrO_8] and / or [CaO_8] [12]. It can be seen that the substitution of Ca^{2+} in the Sr^{2+} sites promotes small changes in the positioning Sr / Ca, In and O atoms and the distance of the Sr-O / Ca-O and In-O atomic bonds, resulting in small distortions in the clusters of [InO_6] and in the cluster of [SrO_8] and / or [CaO_8]. Fig. 4 shows the difference of the distances of the chemical bonds between the Sr-O and Ca-O atoms of the samples.Schenck and Müller-buschbaum [12] presented values close to the distances between the Sr-O atoms of $SrIn_2O_4$shown in Fig. 4, which were 2.53 Å (2x), 2.55 Å (2x), 2.61 Å, 2.69 Å, 2.75 Å and 3.76 Å. The small changes at these distances is a result of the synthesis method used, its temperature and time conditions, and the changes promoted by the substitution of Ca^{2+} in the Sr^{2+} sites.

The morphology of $Sr_{1-x}Ca_xIn_2O_4$ particles (Fig. 5) is microspheres formed by nanoparticles. Fig. 5(a) shows the morphology of $SrIn_2O_4$, it is seen that the microspheres have porous surfaces, such as foam. On the other hand, in Fig. 5(f), the $CaIn_2O_4$ microspheres have a less porous surface. Messing et al. [45] reported some simultaneos physical phenomena during the pyrolysis spray process as the evaporation of the solvent on the surface of the droplet, diffusion of solvent vapors away from the drop in the gas phase, shrinkage of the drop, change in the drop temperature and diffusion of solute towards the center of the drop. Furthermore, it is described that metal nitrate derivatives generally form porous or irregular particles, because the metal nitrates melt before the solvent is completely removed, and the molten salt formed will inhibit the solvent removal [45].

Thus, the use of strontium nitrate favors phenomena that result in the formation of particles with a porous surface, while the use of a higher percentage of calcium nitrate favors the formation of particles with a less rough surface. Kang et al. [46] obtained $SrTiO_3$ particles via spray pyrolysis with spherical morphology and porous surface. While, Lanfredi et al. [47] synthesized $CaTiO_3$ using the pyrolysis spray method, but the particles showed spherical morphology and non-porous surface. Thus, with the increase of x value of $Sr_{1-x}Ca_xIn_2O_4$, there is a decrease in the surface porosity of the particles, due to the stoichiometric increase of calcium and the reduction of strontium, as shown in Fig. 6.

The diffuse reflectance spectroscopy in the visible ultraviolet region was used to determine the gap band of the samples. The reflectance data were converted to absorbance data using the Kubelka-Munk function [48], and the optical gap band value (Egap) was estimated using the Wood and Tauc method [49]. In the Wood and Tauc's method, the optical gap energy is given by $\alpha h\nu\ \alpha\ (h\nu - Egap)\ k$, where h is the Planck constant, ν is the frequency, α is the absorbance and k is indicated for different transitions (k = 1/2, 2, 3/2 or 3 for direct allowed, indirect allowed, direct forbidden and indirect forbidden, respectively). For the $Sr_{1-x}Ca_xIn_2O_4$ samples, k = 2 was allowed, that is, indirect allowed, indicating an indirect allowed electronic transition. Absorbance versus photon energy plot (eV) was plotted and the linear portion of the curve was extrapolated for zero absorption to estimate Egap. Fig. 7 and Table 4 present the estimated values for the gap energy of $Sr_{1-x}Ca_xIn_2O_4$

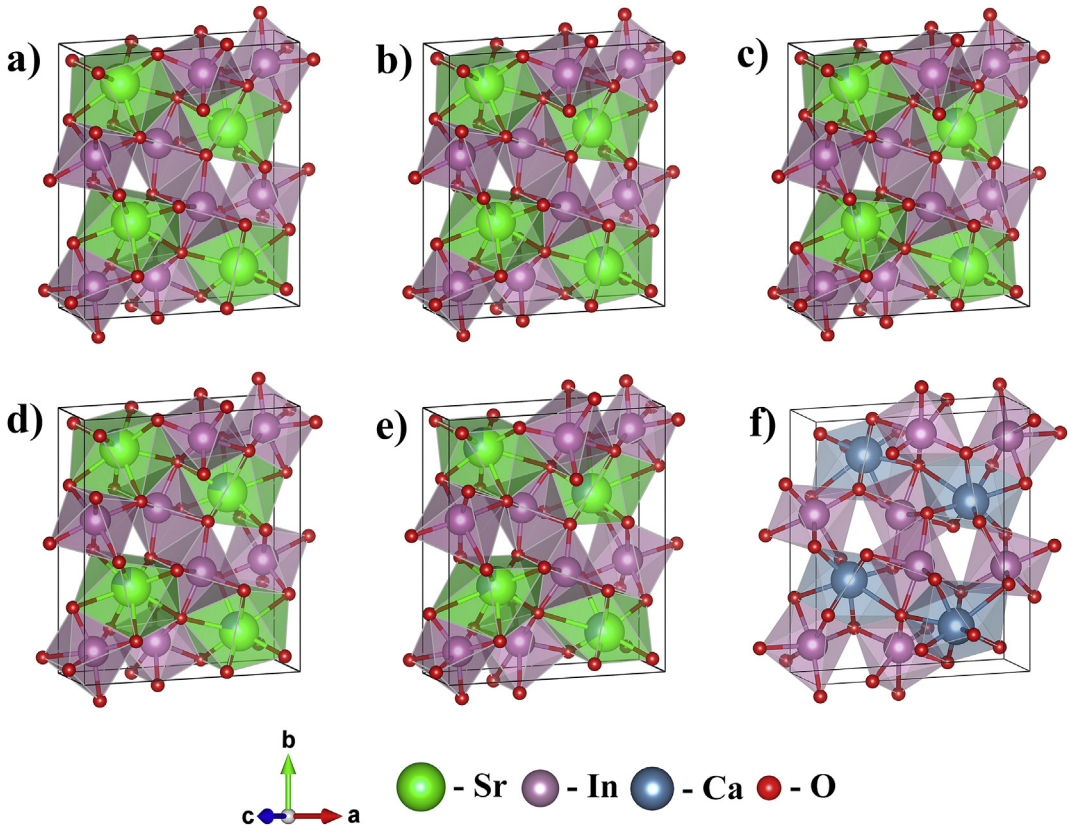

Fig. 3. Model of orthorhombic structure of the (a) $SrIn_2O_4$, (b) $Sr_{0.9}Ca_{0.1}In_2O_4$, (c) $Sr_{0.8}Ca_{0.2}In_2O_4$, (d) $Sr_{0.7}Ca_{0.3}In_2O_4$, (e) $Sr_{0.6}Ca_{0.4}In_2O_4$ and (f) $CaIn_2O_4$.

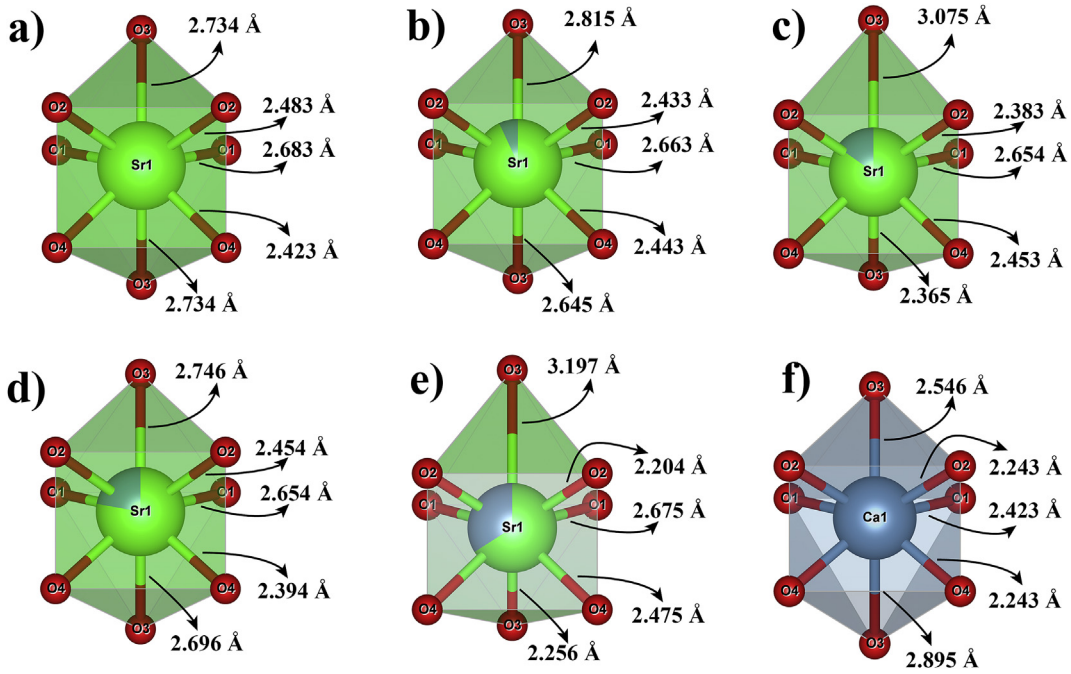

Fig. 4. Distances of the chemical bonds between Sr-O and Ca-O atoms of the (a) $SrIn_2O_4$, (b) $Sr_{0.9}Ca_{0.1}In_2O_4$, (c) $Sr_{0.8}Ca_{0.2}In_2O_4$, (d) $Sr_{0.7}Ca_{0.3}In_2O_4$, (e) $Sr_{0.6}Ca_{0.4}In_2O_4$ and (f) $CaIn_2O_4$.

samples (x = 0, 0.1, 0.2, 0.3, 0.4 and 1 mol %). The verified band gap values of the samples are in agreement with the values found in the literature (Table 4). Dali et al. [50] synthesized $SrIn_2O_4$ and $CaIn_2O_4$ using solid state reaction at 900 °C for 24 h and found that Egap values were 3.60 eV and 3.90 eV, respectively.

The small differences observed in the gap band of the samples can be attributed to the use of the synthesis method, as well as reagents, temperature, time and morphology. It was observed that

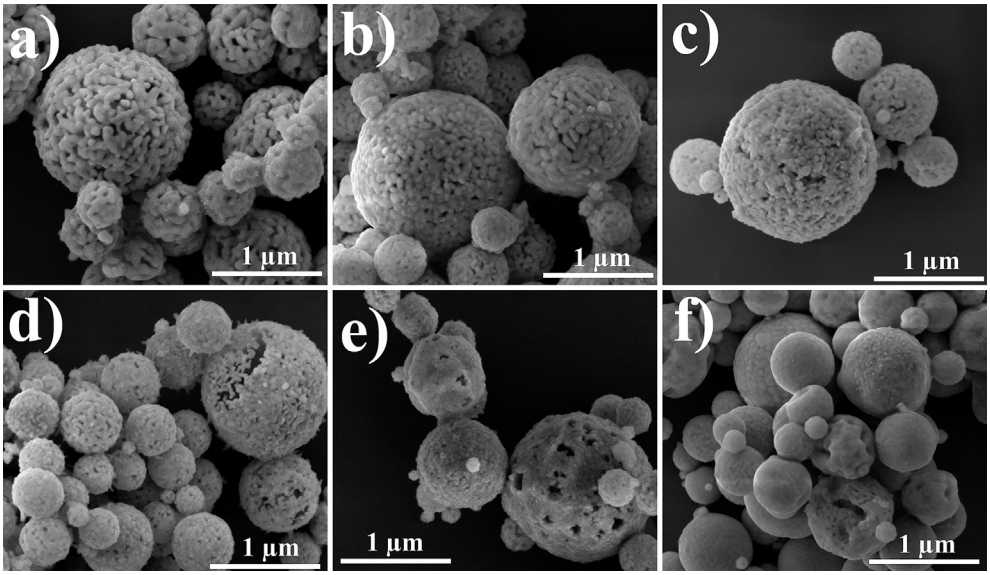

Fig. 5. SEM micrographs of (a) $SrIn_2O_4$, (b) $Sr_{0.9}Ca_{0.1}In_2O_4$, (c) $Sr_{0.8}Ca_{0.2}In_2O_4$, (d) $Sr_{0.7}Ca_{0.3}In_2O_4$, (e) $Sr_{0.6}Ca_{0.4}In_2O_4$and (f) $CaIn_2O_4$.

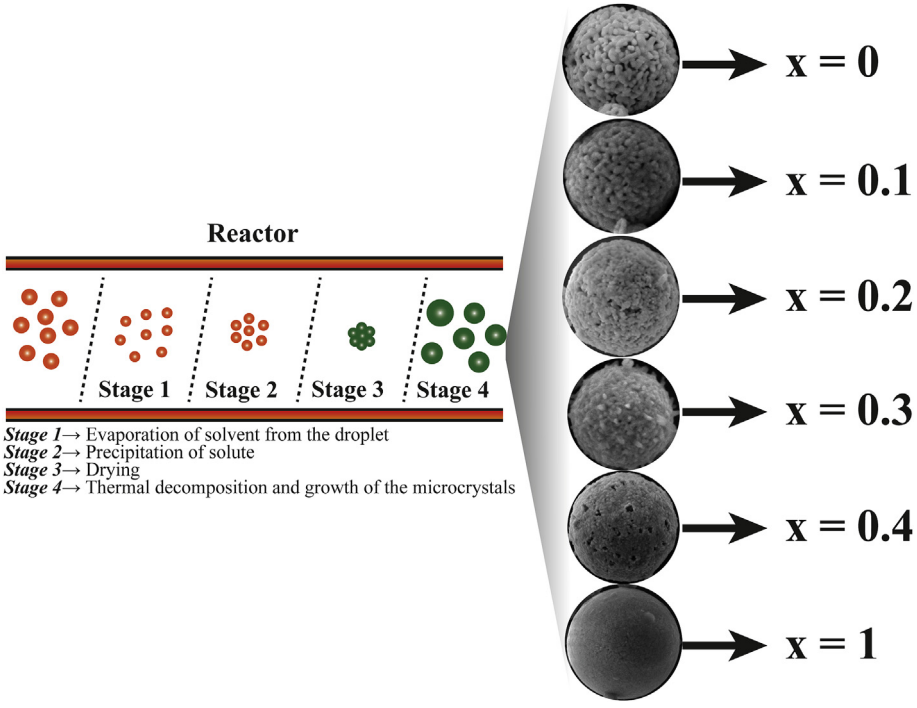

Fig. 6. Illustration of the morphology variation of $Sr_{1-x}Ca_xIn_2O_4$ particles according to the value of x.

the substitution of Sr^{2+} cations for Ca^{2+} cations resulted in a slight decrease in the gap energy, being more evident when x = 0.1. It is believed that the slight decrease in gap energy is related to defects introduced by cationic substitution, as well as displacement of Sr-O / Ca-O and In-O bonds, and distortion of [InO_6] and [SrO_8] clusters / [CaO_8] (Figs. 3 and 4).

Fig. 8 shows the photoluminescent emission (PL) spectra of the $Sr_{1-x}Ca_xIn_2O_4$ (x = 0.1, 0.2, 0.3, 0.4 and 1 mol %) powders obtained by the USP method at room temperature, when excited at 350.7 nm. Spectra are typical of broadband systems where relaxation processes occur by multiphonon and multilevel processes, that is, a system in which relaxation occurs by several paths and involving the participation of numerous intermediate states within the gap band of the materials investigated [51].

A proper structural disorder can result in a better photoluminescent emission compared to a fully ordered structure. In general, structurally disordered materials exhibit oxygen vacancies, network defects, impurities and / or distorted local bonds that give rise to electronic levels in the band gap. These electronic levels are responsible for improving the PL emission process [52].

In the PL emission, each electronic transition is represented by a color and associated with a structural arrangement, the lower the order of this structural arrangement, the more the spectrum tends to decrease in the areas of blue-green and to increase in the areas of

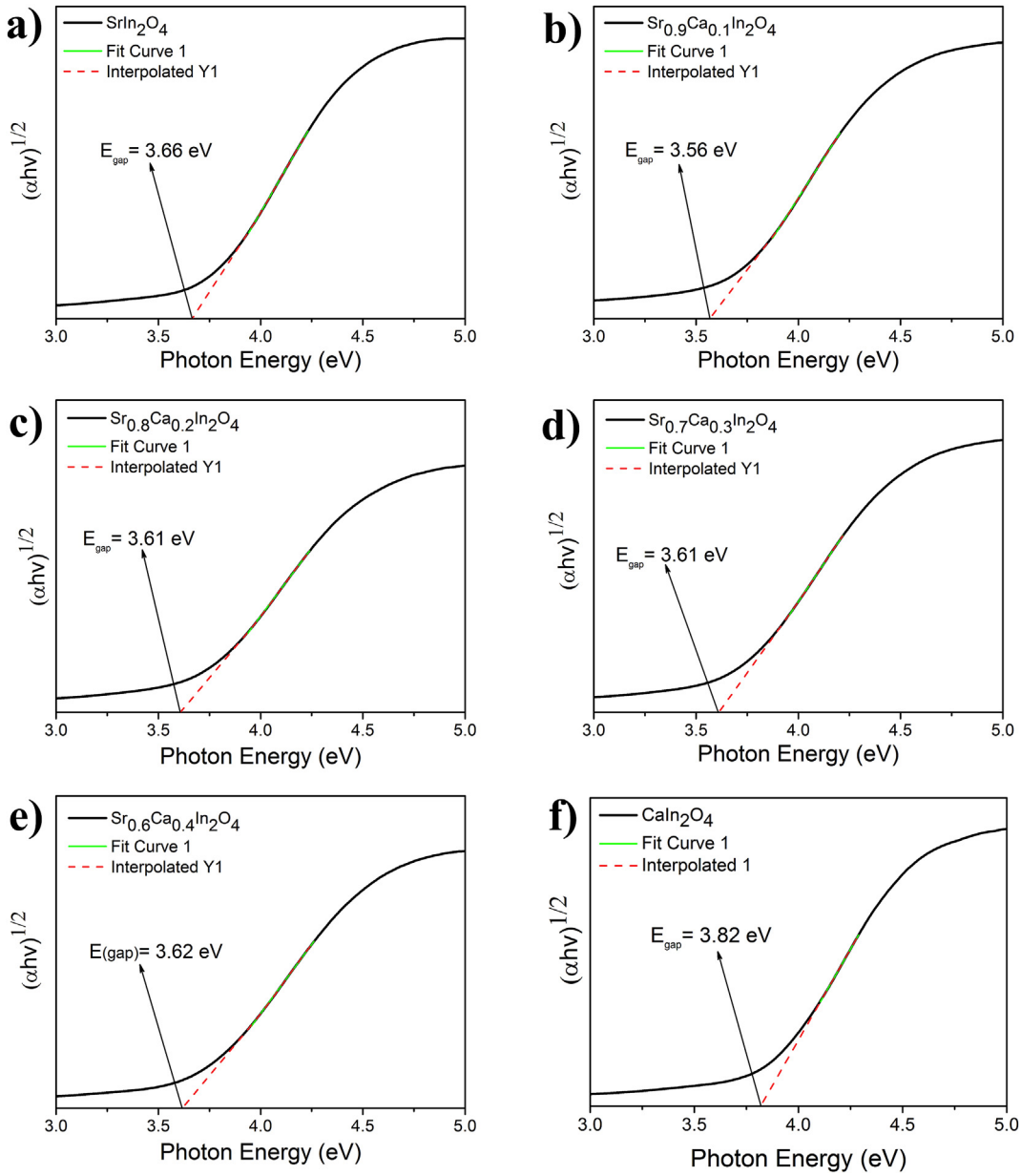

Fig. 7. UV–Vis absorbance spectra of (a) $SrIn_2O_4$, (b) $Sr_{0.9}Ca_{0.1}In_2O_4$, (c) $Sr_{0.8}Ca_{0.2}In_2O_4$, (d) $Sr_{0.7}Ca_{0.3}In_2O_4$, (e) $Sr_{0.6}Ca_{0.4}In_2O_4$and (f) $CaIn_2O_4$.

Table 4
Comparative results between the E_{gap} values of$Sr_{1-x}Ca_xIn_2O_4$ (x = 0, 0.1, 0.2, 0.3, 0.4 and 1) obtained in this work and those reported in the literature.

Sample	E_{gap} (eV)	Synthesis Method	Ref.
$SrIn_2O_4$	3.66	SPU	[This work]
$Sr_{0.9}Ca_{0.1}In_2O_4$	3.56	SPU	[This work]
$Sr_{0.9}Ca_{0.1}In_2O_4$	3.61	SPU	[This work]
$Sr_{0.8}Ca_{0.2}In_2O_4$	3.61	SPU	[This work]
$Sr_{0.7}Ca_{0.3}In_2O_4$	3.61	SPU	[This work]
$Sr_{0.6}Ca_{0.4}In_2O_4$	3.62	SPU	[This work]
$CaIn_2O_4$	3.82	SPU	[This work]
$SrIn_2O_4$	3.60	State Solid	[51]
$CaIn_2O_4$	3.90	State Solid	[51]
$SrIn_2O_4$	3.66	Combustion	[18]
$CaIn_2O_4$	3.46	Combustion	[28]
$CaIn_2O_4$	3.82	SPU	[32]

yellow-orange-red. Therefore, the emission in the blue-green is associated with an orderly structure with shallow defects, while the

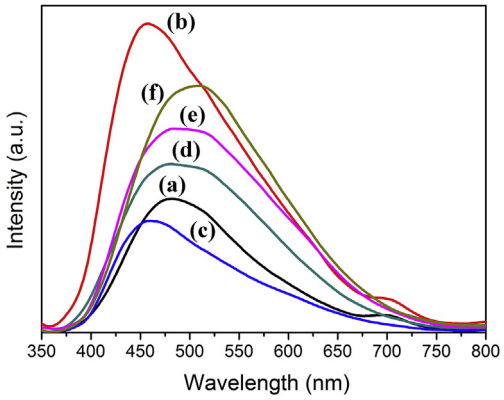

Fig. 8. PL emission spectra of (a) $SrIn_2O_4$, (b) $Sr_{0.9}Ca_{0.1}In_2O_4$, (c) $Sr_{0.8}Ca_{0.2}In_2O_4$, (d) $Sr_{0.7}Ca_{0.3}In_2O_4$, (e) $Sr_{0.6}Ca_{0.4}In_2O_4$ and (f) $CaIn_2O_4$.

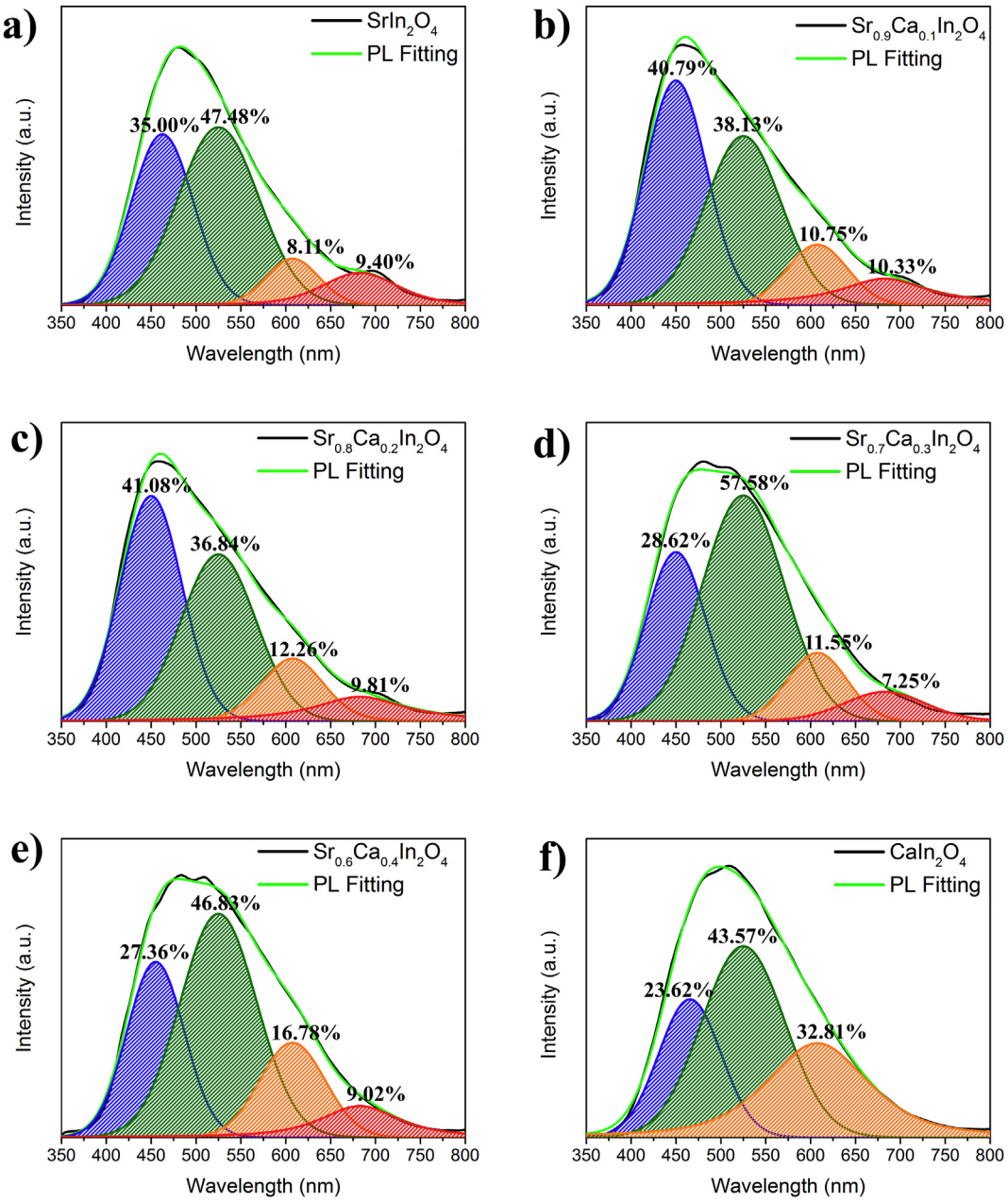

Fig. 9. Deconvolute the PL curves of (a) $SrIn_2O_4$, (b) $Sr_{0.9}Ca_{0.1}In_2O_4$, (c) $Sr_{0.8}Ca_{0.2}In_2O_4$, (d) $Sr_{0.7}Ca_{0.3}In_2O_4$, (e) $Sr_{0.6}Ca_{0.4}In_2O_4$ and (f) $CaIn_2O_4$.

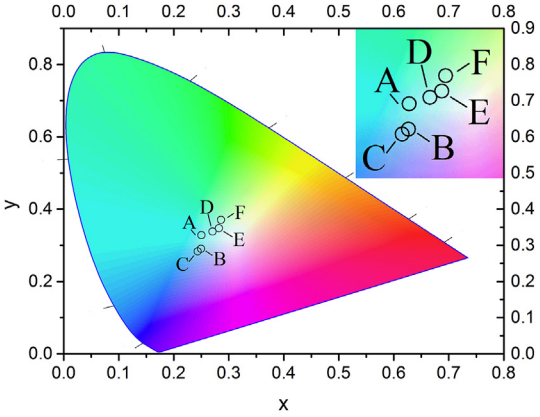

Fig. 10. CIE diagram of$Sr_{1-x}Ca_xIn_2O_4$ (x = 0, 0.1, 0.2, 0.3, 0.4 and 1).

emission in red-yellow is associated with a disordered structure with deep defects [52]. Using the Gaussian method, PL curves of the samples were decomposed into five components, referring to the region in the visible spectrum. PL curves were analyzed using the PeakFit deconvolution program [53]. The features extracted from deconvolution curves and the areas under the curve of respective transitions are illustrated in Fig. 9(a–f).

The $Sr_{1-x}Ca_xIn_2O_4$ PL curves for all samples are composed of four PL components with the following nm maxima: blue = 450 nm, green = 525 nm, orange = 607.5 nm and red = 682.5 nm. The PL deconvolution (Fig. 9) shows the $Sr_{1-x}Ca_xIn_2O_4$ disordered to ordered structure, favoring the green and blue light emission for the all samples.

The x and y coordinates were determined to verify the light emission. The CIE color coordinates can be calculated by integrating the X, Y and Z values [54]. The CIE is one of the important factors to

Table 5
Chromaticity coordinates (CIE) and correlated temperature color (CCT) for $Sr_{1-x}Ca_xIn_2O_4$ (x = 0, 0.1, 0.2, 0.3, 0.4 and 1).

Code	Sample	x	y	CCT (K)	Color
A	$SrIn_2O_4$	0.2503	0.3282	10831	Overcast sky (Blue)
B	$Sr_{0.9}Ca_{0.1}In_2O_4$	0.2496	0.2904	14108	Beginning dusk (Blue)
C	$Sr_{0.8}Ca_{0.2}In_2O_4$	0.2434	0.283	16643	Beginning dusk (Blue)
D	$Sr_{0.7}Ca_{0.3}In_2O_4$	0.2706	0.3379	8883	Cloudy sky (Blue)
E	$Sr_{0.6}Ca_{0.4}In_2O_4$	0.2823	0.3472	7952	Average summer shade (Blue)
F	$CaIn_2O_4$	0.286	0.3703	7420	Light summer shade (Blue)

evaluate the performance of phosphors. Fig. 10 shows the CIE (x, y) coordinates of the samples, while Table 5 lists the CIE coordinate values, color temperature correlation (CCT) values and the emitted color of each sample.

All samples showed light emission in the blue color. However, for samples with x = 0, 0.1 and 0.2 the CCTs were colder than for samples with x = 0.3, 0.4 and 1. This occurs because the samples with x = 0.1 and 0.2 show a predominant emission in the blue region, while the samples with x = 0.3, 0.4 show the largest emission contribution in the green region.

4. Conclusion

The $Sr_{1-x}Ca_xIn_2O_4$ powders (x = 0, 0.1, 0.2, 0.3, 0.4 and 1 mol %) were obtained, in a single step by the ultrasonic pyrolysis spray process. The XRD patterns showed that the samples have an orthorhombic crystal structure, with the network parameters and crystallite size which decreases as the cationic substitution of $Sr^{2+}$for Ca^{2+}increases. The particles obtained are predominantly spherical, with a porous surface in the form of foam for x = 0 and a slightly rough surface for x = 1, observing a decrease of the surface porosity as the values of x increase, that is, with an increase in the replacement of Sr^{2+}ions for Ca^{2+} ions. The gap energy varied between 4.56 eV and 4.86 eV, presenting the lowest energy for the sample with x = 0.1. The spectra of PL emission of the all samples have broadband behavior, with predominant emission in the blue-green region. According to the CIE diagram, the samples have emission in the blue region. These optical properties exhibited by disordered $Sr_{1-x}Ca_xIn_2O_4$ suggest that this material is a highly promising candidate for photoluminescent applications.

Acknowledgments

The authors thank the financial support of the Brazilian research financing institutions: CAPES/PROCAD 2013/2998/2014, CNPq.N° 307546/2014-4, FAPESP2013/07296-2 and INCTMN 2008/57872-1.

References

[1] W.-K. Chang, D.-S. Sun, H. Chan, P.-T. Huang, W.-S. Wu, C.-H. Lin, Y.-H. Tseng, Y.-H. Cheng, C.-C. Tseng, H.-H. Chang, Visible light–responsive core-shell structured In_2O_3@$CaIn_2O_4$ photocatalyst with superior bactericidal properties and biocompatibility, Nanomed. Nanotechnol. Biol. Med. 8 (2012) 609–617.
[2] J.M. Thornton, D. Raftery, Efficient photocatalytic hydrogen production by platinum-loaded carbon-doped cadmium indate nanoparticles, ACS Appl. Mater. Interfaces 4 (2012) 2426–2431.
[3] Y. Wang, S. Xue, P. Xie, Z. Gao, R. Zou, Preparation, characterization and photocatalytic activity of juglans-like indium oxide (In_2O_3) nanospheres, Mater. Lett. 192 (2017) 76–79.
[4] Q. Liu, Y. Liu, B. Gao, Y. Chen, B. Lin, Hydrothermal synthesis of In_2O_3-loaded $BiVO_4$ with exposed {010}{110} facets for enhanced visible-light photocatalytic activity, Mater. Res. Bull. 87 (2017) 114–118.
[5] H. Yang, J. Tian, Y. Bo, Y. Zhou, X. Wang, H. Cui, Visible photocatalytic and photoelectrochemical activities of TiO_2 nanobelts modified by In_2O_3 nanoparticles, J. Colloid Interface Sci. 487 (2017) 258–265.
[6] T. Koida, Y. Ueno, J. Nishinaga, H. Higuchi, H. Takahashi, M. Iioka, H. Shibata, S. Niki, Cu(In,Ga)Se_2 solar cells with amorphous In_2O_3-based front contact layers, ACS Appl. Mater. Interfaces 9 (2017) 29677–29686.
[7] J. Shen, F. Li, B. Yin, L. Sun, C. Chen, S. Wen, Y. Chen, S. Ruan, Enhanced ethyl acetate sensing performance of Al-doped In_2O_3 microcubes, Sensor Actuat. B-Chem. 253 (2017) 461–469.
[8] M. Ding, N. Xie, C. Wang, X. Kou, H. Zhang, L. Guo, Y. Sun, X. Chuai, Y. Gao, F. Liu, P. Sun, G. Lu, Enhanced NO_2 gas sensing properties by Ag-doped hollow urchin-like In_2O_3 hierarchical nanostructures, Sensor Actuat. B-Chem. 252 (2017) 418–427.
[9] L. Jin, X. Zhao, X. Qian, S. Wang, X. Shen, M. Dong, Synthesis of porous In_2O_3/carbon composites derived from metal-organic frameworks for high performance Li-ion batteries, Mater. Lett. 199 (2017) 176–179.
[10] Y. Zhao, R.-J. Xie, B. Dierre, T. Takeda, T. Sekiguchi, N. Hirosaki, L. Wang, Enhanced cathodoluminescence of green β-sialon:Eu^{2+} phosphor by In_2O_3 coating, J. Alloys Compd. 727 (2017) 1110–1114.
[11] V. Singh, M. Seshadri, N. Singh, M.S. Pathak, R.S. Kumaran, Y.-K. Choi, P.K. Singh, S.J. Dhoble, A.K. Srivastava, Optical characterization, absorption and upconversion luminescence in $Er^{3+}$and Er^{3+}/Yb^{3+}doped In_2O_3 phosphor, J. Lumin. 176 (2016) 347–355.
[12] R.V. Schenck, H. Müller-buschbaum, Über Erdalkalimetalloxoindate. III. kristallstrukturuntersuchung an $SrIn_2O_4$, zeitschrift für anorganische und allgemeine, Chem. 398 (1973) 24–30.
[13] M. Guan, H. Zheng, L. Mei, M.S. Molokeev, J. Xie, T. Yang, X. Wu, S. Huang, Z. Huang, Preparation, structure, and up-conversion luminescence of Yb^{3+}/Er^{3+} codoped $SrIn_2O_4$ phosphors, J. Am. Ceram. Soc. 98 (2015) 1182–1187.
[14] Y. Kang, B. Thuy, Y. Shimokawa, T. Hayakawa, S. Sakaida, L. Miao, S. Tanemura, S. Honda, Y. Iwamoto, Relationship between Eu^{3+} substitution sites and photoluminescence properties of $SrIn_2O_4$:Eu^{3+} spinel phosphors, J. Lumin. 169 (Part A) (2016) 78–85.
[15] H. Wang, L. Tian, Luminescence properties of $SrIn_2O_4$:Eu^{3+} incorporated with Gd^{3+} or Sm^{3+} ions, J. Alloys Compd. 509 (2011) 2659–2662.
[16] P. Li, Z. Wang, Z. Yang, Q. Guo, $SrIn_2O_4$:Eu^{3+}, Sm^{3+}: a red emitting phosphor with a broadened near-ultraviolet absorption band for solid-state lighting, J. Electrochem. Soc. 158 (2011) H1201–H1205.
[17] F.-S. Kao, A study on the luminescent properties of new green-emitting $SrIn_2O_4$:xTb phosphor, Mater. Chem. Phys. 76 (2002) 295–298.
[18] S.B. Kokane, S. Sartale, C. Betty, R. Sasikala, Pd–TiO_2–$SrIn_2O_4$ heterojunction photocatalyst: enhanced photocatalytic activity for hydrogen generation and degradation of methylene blue, RSC Adv. 4 (2014) 55539–55547.
[19] J. Tang, Z. Zou, M. Katagiri, T. Kako, J. Ye, Photocatalytic degradation of MB on MIn_2O_4 (M=alkali earth metal) under visible light: effects of crystal and electronic structure on the photocatalytic activity, Catal. Today 93–95 (2004) 885–889.
[20] M. Guan, H. Zheng, Z. Huang, B. Ma, M.S. Molokeev, S. Huang, L. Mei, Ca/Sr ratio dependent structure and up-conversion luminescence of $(Ca_{1-x}Sr_x)In_2O_4$: Yb^{3+}/Ho^{3+} phosphors, RSC Adv. 5 (2015) 59403–59407.
[21] J. Gou, D. Zhang, B. Yu, J. Wang, S. Liu, The photoluminescence behaviors of a novel reddish orange emitting phosphor $CaIn_2O_4$:Sm^{3+} codoped with Zn^{2+} or Al^{3+} ions, J. Nanomater. 14 (2015).
[22] J. Gou, J. Wang, B. Yu, D. Zhang, Synthesis and photoluminescence characteristics of $CaIn_2O_4$:Dy^{3+} phosphors co-doped with Gd^{3+}, Zn^{2+} or Al^{3+} ions, J. Nanosci. Nanotechnol. 16 (2016) 3973–3976.
[23] T. Li, C.-F. Guo, Y.-M. Yang, L. Li, N. Zhang, Efficient green up-conversion emission in Yb^{3+}/Ho^{3+} co-doped $CaIn_2O_4$, Acta Mater. 61 (2013) 7481–7487.
[24] T. Li, C. Guo, L. Li, Up-conversion luminescence of Er^{3+}-Yb^{3+} co-doped $CaIn_2O_4$, Opt. Express 21 (2013) 18281–18289.
[25] M.F.C. Abreu, F.V. Motta, R.C. Lima, M.S. Li, E. Longo, A.P.A. Marques, Effect of process parameters on photophysical properties and barium molybdate phosphors characteristics, Ceram. Int. 40 (2014) 6719–6729.
[26] W. Zhi-Jun, L. Pan-Lai, Y. Zhi-Ping, G. Qing-Lin, Improving luminescent property of $SrIn_2O_4$: Eu^{3+} by co-doped A^+ (A= Li, Na, K) or Sm^{3+}, Chin. Phys. B 22 (2013) 047804.
[27] X. Yan, W. Li, K. Sun, A novel red emitting phosphor $CaIn_2O_4$:Eu^{3+}, Sm^{3+} with a broadened near-ultraviolet absorption band for solid-state lighting, Mater. Res. Bull. 46 (2011) 87–91.
[28] J. Ding, W. Yan, S. Sun, J. Bao, C. Gao, Fabrication of graphene/$CaIn_2O_4$ composites with enhanced photocatalytic activity from water under visible light irradiation, Int. J. Hydrogen Energy 39 (2014) 119–126.
[29] Y. Zhang, R. Selvaraj, M. Sillanpää, Y. Kim, C.-W. Tai, Coprecipitates synthesis of $CaIn_2O_4$ and its photocatalytic degradation of methylene blue by visible light irradiation, Ind. Eng. Chem. Res. 53 (2014) 11720–11726.
[30] H. Zheng, Z. Zhang, J. Zhou, S. Yang, J. Zhao, Vibrational spectra of $CaGa_2O_4$, Ca_2GeO_4, $CaIn_2O_4$ and $CaSnO_3$ prepared by electrospinning, Appl. Phys. A 108

(2012) 465–473.
[31] X. Liu, C. Lin, Y. Luo, J. Lin, Host-sensitized luminescence of Dy^{3+}, Pr^{3+}, Tb^{3+} in polycrystalline SrIn2O4 for field emission displays, J. Electrochem. Soc. 154 (2007) J21–J27.
[32] M.T.S. Tavares, M.M. Melo, V.D. Araújo, R.L. Tranquilin, C.R.R. Almeida, C.A. Paskocimas, M.R.D. Bomio, E. Longo, F.V. Motta, Enhancement of the photocatalytic activity and white emission of $CaIn_2O_4$ nanocrystals, J. Alloys Compd. 658 (2016) 316–323.
[33] S. Lin, K. Borgohain, W. Wei, Praseodymium-doped photo-luminescent strontium indate nanoparticles by ultrasonic spray pyrolysis, J. Am. Ceram. Soc. 89 (2006) 3266–3269.
[34] P. Majerič, D. Jenko, B. Friedrich, R. Rudolf, Formation mechanisms for gold nanoparticles in a redesigned Ultrasonic Spray Pyrolysis, Adv. Powder Technol. 28 (2017) 876–883.
[35] Z. Cheng, P. Foroughi, A. Behrens, Synthesis of nanocrystalline TaC powders via single-step high temperature spray pyrolysis from solution precursors, Ceram. Int. 43 (2017) 3431–3434.
[36] C.R.R. Almeida, L.X. Lovisa, A.A.G. Santiago, M.S. Li, E. Longo, C.A. Paskocimas, F.V. Motta, M.R.D. Bomio, One-step synthesis of $CaMoO_4$:Eu^{3+} nanospheres by ultrasonic spray pyrolysis, J. Mater. Sci.-Mater. El. 28 (2017) 16867–16879.
[37] A.A.G. Santiago, C.R.R. Almeida, R.L. Tranquilin, R.M. Nascimento, C.A. Paskocimas, E. Longo, F.V. Motta, M.R.D. Bomio, Photoluminescent properties of the $Ba_{1-x}Zn_xMoO_4$ heterostructure obtained by ultrasonic spray pyrolysis, Ceram. Int. 44 (2018) 3775–3786.
[38] S.D. Ramarao, S.R. Kiran, V.R.K. Murthy, Structural, lattice vibrational, optical and microwave dielectric studies on $Ca_{1-x}Sr_xMoO_4$ ceramics with scheelite structure, Mater. Res. Bull. 56 (2014) 71–79.
[39] H. Rietveld, A profile refinement method for nuclear and magnetic structures, J. Appl. Crystallogr. 2 (1969) 65–71.
[40] B. Toby, EXPGUI, a graphical user interface for GSAS, J. Appl. Crystallogr. 34 (2001) 210–213.
[41] N. Lakshminarasimhan, U.V. Varadaraju, Role of crystallite size on the photoluminescence properties of $SrIn_2O_4$:Eu^{3+} phosphor synthesized by different methods, J. Solid State Chem. 181 (2008) 2418–2423.
[42] M.J. McKelvy, R. Sharma, A.V.G. Chizmeshya, R.W. Carpenter, K. Streib, Magnesium hydroxide dehydroxylation: in situ nanoscale observations of lamellar nucleation and growth, Chem. Mater. 13 (2001) 921–926.
[43] F.V. Motta, A.P.A. Marques, M.S. Li, M.F.C. Abreu, C.A. Paskocimas, M.R.D. Bomio, R.P. Souza, J.A. Varela, E. Longo, Preparation and photoluminescence characteristics of $In(OH)_3$:xTb^{3+} obtained by Microwave-Assisted Hydrothermal method, J. Alloys Compd. 553 (2013) 338–342.
[44] K. Momma, F. Izumi, VESTA 3 for three-dimensional visualization of crystal, volumetric and morphology data, J. Appl. Crystallogr. 44 (2011) 1272–1276.
[45] G.L. Messing, S.-C. Zhang, G.V. Jayanthi, Ceramic powder synthesis by spray pyrolysis, J. Am. Ceram. Soc. 76 (1993) 2707–2726.
[46] H.W. Kang, S.B. Park, A.-H.A. Park, Effects of charge balance with Na^+ on $SrTiO_3$:Mo^{6+} prepared by spray pyrolysis for H_2 evolution under visible light irradiation, Int. J. Hydrogen Energy 38 (2013) 9198–9205.
[47] S. Lanfredi, F. Storti, L.P.M. Simões, E. Djurado, M.A.L. Nobre, Synthesis and structural characterization of calcium titanate by spray pyrolysis method, Mater. Lett. 201 (2017) 148–151.
[48] L. Tolvaj, K. Mitsui, D. Varga, Validity limits of Kubelka–Munk theory for DRIFT spectra of photodegraded solid wood, Wood Sci. Technol. 45 (2011) 135–146.
[49] D.L. Wood, J. Tauc, Weak absorption tails in amorphous semiconductors, Phys. Rev. B 5 (1972) 3144–3151.
[50] S. Esther Dali, V.V.S.S. Sai Sundar, M. Jayachandran, M.J. Chockalingam, Synthesis and characterization of AIn_2O_4 indates, A = Mg, Ca, Sr, Ba, J. Mater. Sci. Lett. 17 (1998) 619–623.
[51] V.M. Longo, L.S. Cavalcante, A.T. de Figueiredo, L.P.S. Santos, E. Longo, J.A. Varela, J.R. Sambrano, C.A. Paskocimas, F.S. De Vicente, A.C. Hernandes, Highly intense violet-blue light emission at room temperature in structurally disordered $SrZrO_3$ powders, Appl. Phys. Lett. 90 (2007) 091906.
[52] A.P.A. Marques, F.V. Motta, M.A. Cruz, J.A. Varela, E. Longo, I.L.V. Rosa, $BaMoO_4$:Tb^{3+} phosphor properties: synthesis, characterization and photophysical studies, Solid State Ionics 202 (2011) 54–59.
[53] T. Ding, W.T. Zheng, H.W. Tian, J.F. Zang, Z.D. Zhao, et al., Temperature-dependent photoluminescence in $La_{2/3}Ca_{1/3}MnO_3$, Solid State Commun. 132 (2004) 815–819.
[54] C. S. McCamy. Correlated Color Temperature as an Explicit Function of Chromaticity Coordinates, Wappingers Falls, New York 12590-1804.